Laminated Permanent Magnets Enable Compact Magnetic Components in Current-Source Converters

Zheng An, *Student Member, IEEE*, Xiangyu Han, *Member, IEEE*, Mickael J. Mauger, *Student Member, IEEE*, Brad Houska, *Student Member, IEEE*, Decheng Yan, *Student Member, IEEE*, Aniruddh Marellapudi, *Student Member, IEEE*, Joseph Benzaquen, *Member, IEEE*, Rajendra Prasad Kandula, *Member, IEEE*, and Deepak Divan, *Life Fellow, IEEE*

***Abstract*—Magnetic components have become one of the primary barriers to high power density converters, especially to current-source converters (CSCs). In CSCs, the inductors/transformers have a predominantly dc flux to store energy, which can be offset by standard permanent magnets (PMs). However, eddy currents in standard PMs induce significant losses and thermal stress for medium-frequency applications. This article proposes using laminated PMs to offset the dc flux while reducing eddy currents, leading to significant reductions in the size, cost, and losses of inductors/transformers. Furthermore, the laminated PMs' optimal location, orientation, and distribution are investigated to generalize this approach for maximum benefits. Three-dimensional finite-element analysis simulation and hardware experiments are presented to validate the effectiveness of the proposed approach in a medium-frequency transformer (MFT) for CSCs. Compared with standard PMs, the proposed use of laminated PMs reduces aggregate core-plus-PM losses by 85% in experiments, and thus, relaxes the MFT thermal design. Finally, the proposed approach is experimentally validated in a 40 kVA flyback-type MFT for a soft-switching solid-state transformer. Compared to the traditional design without any PMs, the proposed design increases the saturation current by 46% while inducing only 5% more losses, leading to significant savings in magnetics cost and size.**

***Index Terms*—Current-source converters (CSCs), dc bias, eddy-current losses, flyback transformers, permanent magnets (PMs), medium-frequency transformers.**

Manuscript received February 8, 2022; revised April 28, 2022; accepted May 10, 2022. Date of publication May 16, 2022; date of current version June 24, 2022. This work was supported in part by the U.S. Department of Energy's Office of Energy Efficiency and Renewable Energy (EERE) under the Solar Energy Technologies Office Award DE-EE0008351 and in part by the Center for Distributed Energy (CDE) at Georgia Tech. Recommended for publication by Associate Editor M. Chen. *(Corresponding author: Zheng An.)*

Zheng An, Mickael J. Mauger, Brad Houska, Decheng Yan, Aniruddh Marellapudi, Joseph Benzaquen, and Deepak Divan are with the Center for Distributed Energy, Georgia Institute of Technology, Atlanta, GA 30332 USA (e-mail: zheng.an@gatech.edu; mickael.mauger@gatech.edu; bhouska3@gatech.edu; decheng.yan@gatech.edu; am123@gatech.edu; jbenzaquen@gatech.edu; ddivan@gatech.edu).

Xiangyu Han was with the Center for Distributed Energy, Georgia Institute Tech, Atlanta, GA 30332 USA, He is now with Tesla Inc., Palo Alto, CA 94304 USA (e-mail: hxy0623@gatech.edu).

Rajendra Prasad Kandula was with the Center for Distributed Energy, Georgia Tech, Atlanta, GA 30332 USA. He is now with the Oak Ridge National Laboratory, Oak Ridge, TN 37831-2008 USA (e-mail: krprasad@gmail.com).

Color versions of one or more figures in this article are available at https://doi.org/10.1109/TPEL.2022.3175388.

Digital Object Identifier 10.1109/TPEL.2022.3175388

I. Introduction

In RECENT years, current-source converters (CSCs) are attracting increasing attention, primarily owing to their enhanced friendliness to short-circuit faults, low dv/dt, electromagnetic interference (EMI), and common-mode voltage when compared with voltage-source converters (VSCs), especially with increased switching frequency by using wide-bandgap devices [1]–[14]. Nonisolated and isolated CSCs have been researched for various applications such as motor drives [1]–[4], electric vehicle (EV) chargers [5], [6], renewable energy integration [7]–[11], and solid-state transformers [12]–[14], among others. In [12], a solid-state transformer based on flyback topology referred to as soft-switching solid-state transformer (S4T) was proposed and an improved version with reduced losses was proposed in [15].

In CSCs, the dc-link energy is stored in the magnetics, either inductors in nonisolated converters or transformer magnetizing inductance of isolated ones, which have become one of the primary barriers to high power density converters. As energy storage elements, dc-link magnetics are crucial to the operation of CSCs and play a critical role in determining the size, cost, and efficiency of the converter. In medium-frequency (i.e., 10–25 kHz) medium-power and high-power applications, nanocrystalline cores are commonly used, thanks to their high saturation flux density, low loss density, high permeability, and high temperature range [16]–[18]. However, they are significantly more costly than amorphous or laminated steel cores. Hence, a reduction in core size is of great interest to the cost reduction of the overall converter. Moreover, a smaller transformer is highly desired for the isolated S4T to minimize the leakage inductance, which negatively affects the peak voltage stress across semiconductor devices [19].

To store energy while facilitating controllability, the magnetics in CSCs have a predominantly high dc flux superimposed on an ac flux at the switching frequency, which also applies to filter inductors in dc applications. Since the size of the magnetic components is determined by the peak flux, a reduction in the dc flux can lead to size reduction. In addition, the dc flux bias increases core losses, which further justifies the necessity of reducing the dc flux in the magnetics [17], [20], [21]. In [22], standard permanent magnets (PMs) were proposed to offset the dc flux, reducing the effective dc flux in the inductor/transformer

cores. These PMs are typically located next to the air gap, leading to a reduction of 63% in transformer size. However, in medium-frequency (MF) applications, the fringing flux around the air gap will induce eddy currents in the PMs, resulting in increased losses in the PMs and MF transformers (MFT) [23]–[25]. Consequently, the PMs can suffer high peak temperatures, affecting their magnetic properties and ultimately resulting in thermal demagnetization or thermal runaway in the worst case.

The losses of PMs are also a challenge to permanent magnet synchronous motors (PMSMs), which usually operate at several hundreds of hertz. Laminated PMs have been explored for PMSMs, and their associated hysteresis and eddy-current losses have been investigated [26]–[29]. In PMSMs, the hysteresis losses, which are proportional to B^2, could be larger than eddy-current losses and cannot be neglected [27]. However, it might not be the case for MF applications, where eddy-current losses, which are proportional to f^2, are supposed to be predominant. This issue has not been researched in the existing literature and was first examined by the same authors in [30].

In this article, using the S4T as an example, 3-D finite-element analysis (3-D-FEA) simulation and experimental results are presented to show the impact of eddy currents in standard block PMs when used with an MFT. The excessive eddy-current losses in standard PMs significantly compromise their benefits of offsetting dc flux bias and prevent them from wide application in practice. Instead, using laminated PMs is proposed to realize the benefits of offsetting the dc flux while reducing eddy currents in MF applications, resulting in reduced size, cost, and losses of inductors/transformers in CSCs. Furthermore, the impact of location and orientation of the PMs to the MFT core on MFT losses is also explored, leading to a generalized minimum-loss design with laminated PMs. The effectiveness of the proposed approach has been validated by both 3-D-FEA simulation and experiments. Finally, the proposed approach is verified in a 40 kVA S4T MFT. Compared to the traditional design without any PMs, the proposed design increases the saturation current by 46% while inducing only 5% more MFT losses, leading to significant savings in magnetics cost and size.

As an extended version of the conference paper in [30], this article contains 3-D-FEA simulation results to validate the proposed approach. It also provides additional insights into loss breakdown and a saturation effect of magnetic flux provided by multiple stacked PMs, helping quantify and analyze the experimental results. Moreover, a comparative study of a 40 kVA S4T MFT was conducted to validate the significant advantages of the proposed design over the traditional design.

This article is organized as follows. Section II introduces the hybrid MFT design with standard PMs in the S4T converters. Section III summarizes thermal characterization results of a 25 kVA S4T MFT with standard PMs. In Section IV, the loss mechanisms of hybrid MFT with PMs are analyzed and the use of laminated PMs for the S4T MFT is proposed to reduce the losses. Section V shows the 3D-FEA simulation results in ANSYS Maxwell. Experimental results are presented in Section VI. Section VII validates the advantages of using laminated PMs in reducing size, cost, and losses of the S4T MFT. Finally, Section VIII concludes this article.

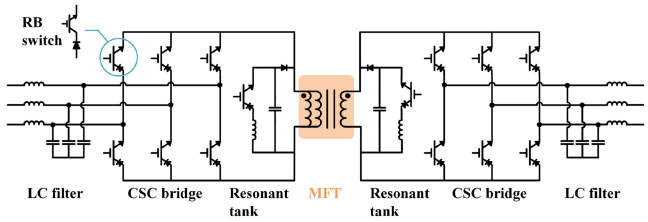

Fig. 1. Circuit schematic of the S4T, a single-stage CSC with ZVS capability. The magnetizing inductance of the MFT acts as an energy storage element and features a dc flux bias.

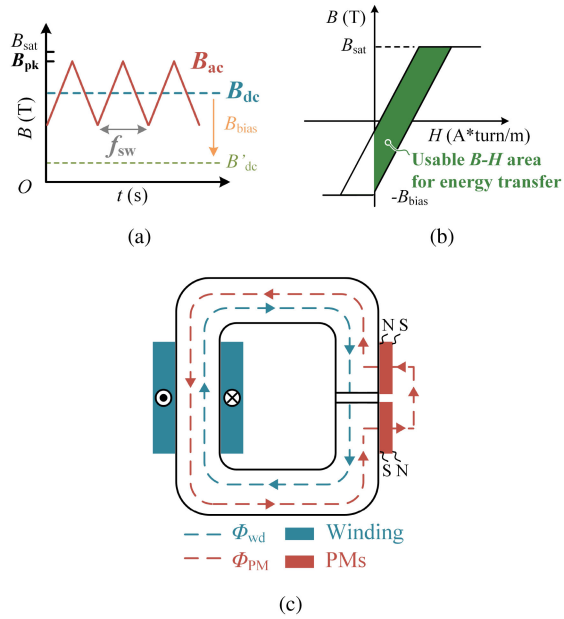

Fig. 2. (a) Typical flux density profile in the S4T MFT with a dc flux superimposed with an ac flux ripple at switching frequency. (b) Usable *B*–*H* area extended to the 3rd quadrant by adding B_{bias}. (c) Hybrid S4T MFT with B_{bias} provided by standard PMs.

II. Hybrid MFT Design With Standard PMs in S4T

This section briefly introduces the S4T converter and the hybrid MFT design with PMs in S4T converters. The schematic of the S4T is shown in Fig. 1. It consists of two current source bridges interconnected through an MFT and auxiliary resonant tanks to enable zero-voltage-switching (ZVS) [12], [15].

The basic operation of S4T is similar to that of a flyback converter. In a certain portion of the switching cycle, one of the bridges transfers energy from power sources to the transformer magnetizing inductance, L_{m}. In the rest of the switching cycle, the other bridge transfers energy from the L_{m} to the loads. The L_{m} acts as an energy storage element and features a dc flux bias much like a flyback converter. It is desirable to keep the transformer size small not only to reduce the cost and losses of the MFT but also to minimize the leakage inductance as it affects the peak voltage stress in the converter negatively [19].

Fig. 2(a) shows the flux density B in the MFT of S4T. It consists of a dc flux, B_{dc}, superimposed by an ac flux, B_{ac}, with a switching frequency of 16–20 kHz. The core material and peak flux B_{pk} determine the transformer size and the value of L_{m}, which is typically designed to keep the peak-peak current

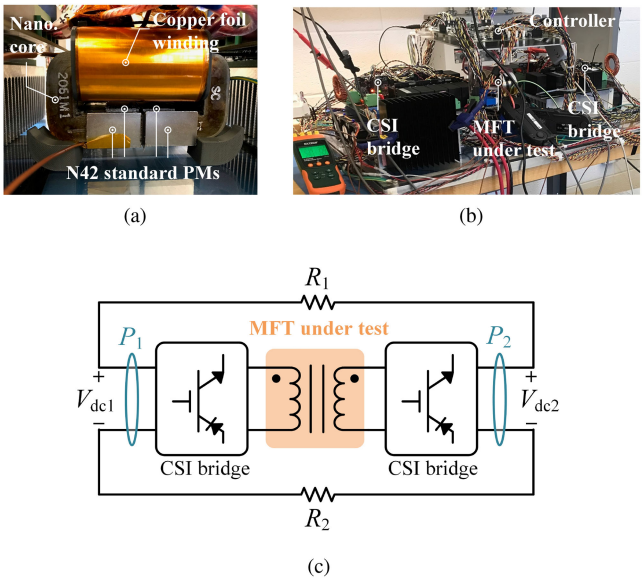

Fig. 3. Loss characterization of the 25 kVA S4T MFT with N42 standard PMs. (a) 25 kVA S4T MFT under test, built by nanocrystalline cores with N42 standard PMs to create dc bias and copper foil windings. (b) Picture of the test setup for thermal characterization. (c) Schematic of thermal characterization test of the S4T MFT.

TABLE I
BOM OF THE 25 KVA S4T MFT

Component	Manufacturer	Part Number
Nanocrystalline core	MK Magnetics	SC2062M1
Standard PMs	K&J Magnetics	BY0X02
Copper foil	Basic Copper	$0.216'' \times 3'' \times 100'$

ripple in the range of 0.4–0.6 p.u. Continued reduction in L_m will increase the current ripple and impact the controllability.

Nanocrystalline cores are typically used in this frequency range (10–25 kHz) to limit the core losses, and they have a peak magnetic flux density of > 1 T [16], [17]. Hence, reducing the effective peak flux B_{pk} is the only remaining degree of freedom to reduce the transformer size. As shown in Fig. 2(a) and Fig. 2(b), the peak flux can be reduced by offsetting B_{dc} using B_{bias}. This can be implemented either by using another dc winding or through PMs. Since additional dc winding will increase transformer size and losses, PMs are typically preferred.

An ideal location for these PMs to create the dc flux bias is in the air gap. However, placing the PMs in the air gap may cause demagnetization during fault conditions [31]. As a result, these PMs are typically placed next to the air gap, as shown in Fig. 2(c). This approach was shown to reduce the transformer size by 60%–70% [22]. However, in practice, these standard PMs heat up when operated as part of the converter, which will be described in the next section.

III. THERMAL PERFORMANCE OF THE S4T MFT WITH STANDARD PMS: EXPERIMENTAL ASSESSMENT

In this section, experiment results are presented to demonstrate the thermal performance of the 25 kVA MFT with standard PMs while operating as a part of the S4T converter.

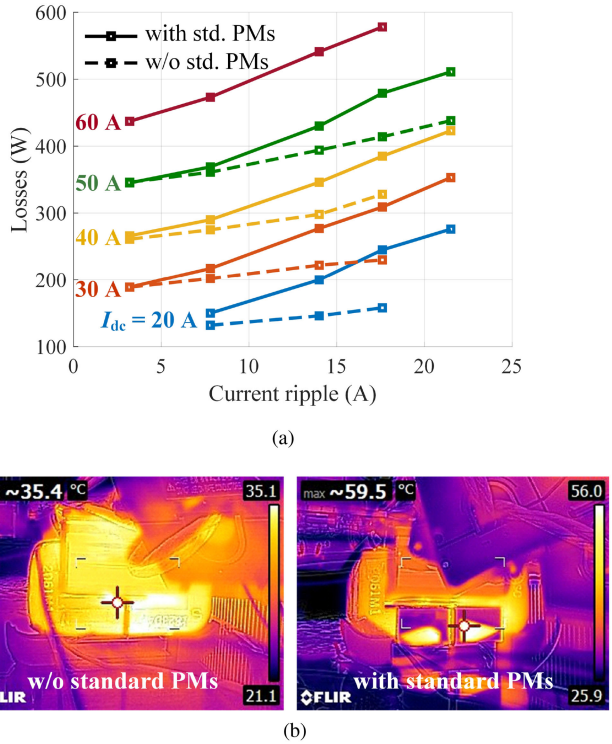

Fig. 4. Thermal performance of the 25 kVA S4T converter with MFT. (a) Converter losses (including MFT with/without PMs) under different dc-link currents and ac current ripples. The increased losses primarily come from added standard PMs. (b) Thermal images of the S4T MFT under test. Hot spots in PMs presents $\sim 70\%$ higher temperature than the case without PMs.

A. Design of a 25-kVA S4T MFT With Standard PMs

Fig. 3(a) shows the picture of a $25\,\text{kVA}/480\,\text{V}$ S4T MFT with standard PMs in block shape and copper foils as per design in [22]. Its bill of materials (BOM) is summarized in Table I. The MFT was built with a pair of nanocrystalline cores from MK Magnetics [32] and standard N42 block magnets of Neodymium-Iron-Boron (NdFeB) material [33] to create the desired bias. Fig. 3(b) and (c) shows the image and the schematic of the experimental setup, which was originally built to test the thermal performance of the S4T converter including the MFT.

B. Thermal Characterization of the 25-kVA S4T MFT

To characterize the impact of PMs on the MFT losses, a set of comparative experiments at multiple dc-link magnetizing currents, I_{dc}, were conducted with the test setup shown in Fig. 3(b), one with standard PMs added to the MFT and the other without them.

Fig. 4(a) presents the comparative experimental results with I_{dc} ranging from 20 A to 60 A, where the converter losses increased dramatically when standard PMs are added to the MFT. with the same current flowing through the converter in two cases, the losses in all components except the MFT, including semiconductor devices, filters, snubbers, etc., should be the

same. As a result, it can be concluded that the increase in converter losses comes from the MFT and is primarily contributed by adding standard PMs to the MFT.

Fig. 4(b) shows the thermal image of the standard PMs, indicating high concentrated heat loss in this region. It is well known that fringing flux will be induced around the air gap of the magnetic cores, resulting in decreased air gap reluctance, additional winding losses, and extra core losses [16], [24], [25]. In the hybrid S4T MFT, the PMs are placed right next to the air gap, where significant fringing flux is expected. Therefore, eddy currents will be induced in the PMs by the fringing flux, leading to increased losses in the PMs. To mitigate the impact of fringing flux on PMs losses, the PMs could be moved away from the air gap with the penalty of a reduced amount of bias they provide to the core. As a result, a viable solution is required to reduce the losses while not sacrificing the flux bias provided by the PMs.

IV. Core Losses With PMs and Proposed Use of Laminated PMs

From the previous section, we learned that adding standard PMs to the MFT will cause significantly more losses in the MFT. In this section, the loss mechanism of the MFT with standard PMs will be analyzed in detail. To reduce the losses, the use of laminated PMs is proposed.

Owing to the strong magnetic coupling between the MFT core and added PMs, core losses and PM losses will be the focus of this article while the winding losses are out of scope. For the convenience of discussion, from this section on, a new term core-plus-PM losses is coined and used to refer to total losses in the MFT core and PMs, while core losses only refer to the losses in the MFT core as conventional practice.

A. Core Losses in Conventional MFT Without PMs

Generally, the core losses consists of two parts: hysteresis losses and eddy-current losses. The hysteresis losses are proportional to $B-H$ loop area and excitation frequency f. They dominate in a low frequency of less than a few kilohertz and can be calculated by

$$P_{\mathrm{h}} = k_{\mathrm{h}} \cdot f \cdot B^2. \tag{1}$$

In comparison, eddy-current losses are proportional to $(f \cdot B)^2$ as in (2), playing an increasingly significant role once the frequency rises to tens and hundreds of kilohertz [16]

$$P_{\mathrm{e}} = k_{\mathrm{e}} \cdot (f \cdot B)^2. \tag{2}$$

In (1) and (2), k_{h} and k_{e} are waveform coefficients of excitation voltage, f is the operating frequency of the core, and B is the magnitude of AC flux density in the core.

In conventional transformers without PMs, total core loss density P_{core} under sinusoidal excitation can be calculated by empirical Steinmetz equation with

$$P_{\mathrm{core}} = P_{\mathrm{h}} + P_{\mathrm{e}} = k \cdot f^{\alpha} \cdot B^{\beta}. \tag{3}$$

For various types of core materials, three compound coefficients k, α, and β will be provided by manufacturers to help characterize total core losses under sinusoidal excitation [16], [17], [34], [35]. For the selected nanocrystalline core operating in the frequency range $[10\,\mathrm{kHz},\ 500\,\mathrm{kHz}]$, the coefficients have been characterized to be $k = 8$, $\alpha = 1.621$, and $\beta = 1.982$, which accounts for both hysteresis and eddy-current losses. An additional flux waveform coefficient of $\pi/4$ was multiplied to calibrate the losses under triangular flux waveform [17].

B. Core Losses in the S4T MFT With Standard PMs

In the S4T MFT with PMs, the core losses can still be estimated with (3) except the flux density in the core (affected by the dc flux bias) changes with added PMs. In addition, extra losses are induced in the PMs owing to the fringing flux around the air gap. Since the strong magnetic coupling between the core and PMs is hardly decoupled in experiments, the total losses in the core and PM are considered as a whole in this article, which is referred to as core-plus-PM losses for the convenience of discussions. As a result, the core-plus-PM losses are subjected to two factors: dc flux bias in the core and fringing flux around the air gap. Both factors would be affected once PMs are added to the S4T MFT. The dc flux bias would become the net dc flux of windings and added PMs, and the fringing flux distribution pattern is subjected to how and where the PMs are placed.

By adding PMs next to the air gap of the MFT core, as depicted in Fig. 2(c), the net dc flux bias in the core decreases, leading to a reduction in core losses [21]. In addition, the selected nanocrystalline core features a lamination structure, making it vulnerable to fringing flux around the air gap. As illustrated in Fig. 5(a), the fringing flux will intersect the core lamination around the air gap [17], [23]. As a result, extra fringing losses, mostly eddy-current losses, will be induced in the core and thus increase the core losses [16], [25].

On the other hand, the losses in the PMs are primarily determined by the fringing flux. By placing the PMs next to the air gap, the fringing flux will intersect the PMs and thus induce eddy currents in them. Consequently, eddy-current losses are generated in the PMs, resulting in hotspots and eventually thermal runaway in the worst case. In the meantime, different placements of the PMs, including their location, orientation to the core, and the distance from the air gap, will affect the fringing flux distribution and thus impact the induced eddy-current losses in the PMs themselves. Generally, the fringing flux density decreases with increased distance from the air gap, leading to reduced eddy-current losses. However, the amount of bias provided by the PMs will also decrease in this case, making it difficult to quantify the consequence.

Despite the uncertain effect of the added PMs on overall core-plus-PM losses, the total eddy-current losses in the core and the PMs are expected to dominate the core-plus-PM losses in the S4T MFT operating around 20 kHz. As a recognized solution to reduce the eddy-current losses, electrically insulated lamination has been widely used in line-frequency transformers made of electrical steel and been preliminarily researched in

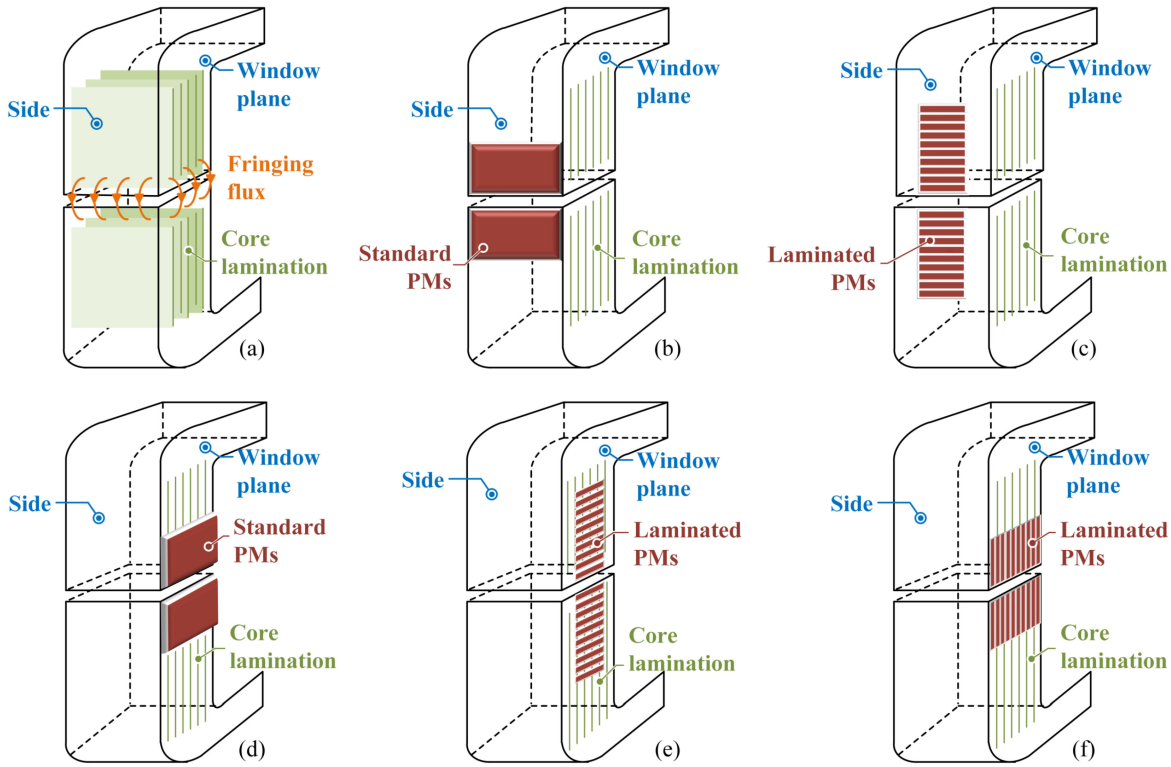

Fig. 5. Different configurations of standard and laminated PMs of research interest. (a) Conventional MFT design without any PMs (base case). (b) Standard PMs on the side (initial design of the S4T MFT). (c) Laminated PMs on the side. (d) Standard PMs on the window plane. (e) Laminated PMs on the window plane. (f) Laminated PMs on the window plane with aligned lamination between PMs and core.

PMSMs [26]–[29]. However, its performance in MF inductors/transformer of CSCs has not been investigated in the existing literature. Taking the S4T MFT as an example, the impact of laminated PMs on the core-plus-PM losses of the S4T MFT is investigated in this article.

C. Proposed Use of Laminated PMs to Reduce Losses

Eddy currents flow in the plane perpendicular to the magnetic flux density $\boldsymbol{B}$. By using laminated structure, the eddy-current losses can be reduced by $1/k^2$, where k is the number of lamination layers [16], [36].

The induced voltage in a conductor by the magnetic field, which drives the eddy current, can be calculated by Faraday's law by

$$v(t) = \frac{d\phi}{dt} = \frac{d(A \cdot B)}{dt} = A \cdot \frac{dB}{dt} \tag{4}$$

where A is the area of the conductor. The resistance of the conductor is calculated by $R = \rho \cdot l/A$. As a result, the eddy-current losses in a conductor P_1 can be calculated by Ohm's law with

$$P_1 = \frac{v^2}{R} = \frac{A^2}{R} \cdot \left(\frac{dB}{dt}\right)^2 \tag{5}$$

with k lamination layers in the same conductor, the area in each layer decreases by k, i.e., $A_\mathrm{k} = A/k$, resulting in an increased $R_\mathrm{k} = k \cdot R$ in each layer. Hence, the total eddy-current losses of k lamination layers P_k can be calculated by

$$\begin{aligned} P_\mathrm{k} &= k \cdot \frac{v_\mathrm{k}^2}{R_\mathrm{k}} = k \cdot \frac{A_\mathrm{k}^2}{R_\mathrm{k}} \cdot \left(\frac{dB}{dt}\right)^2 \\ &= k \cdot \frac{(A/k)^2}{k \cdot R} \cdot \left(\frac{dB}{dt}\right)^2 \\ &= \frac{P_1}{k^2}. \end{aligned} \tag{6}$$

This article proposes the use of laminated PMs in the S4T MFT operating between 15–20 kHz to reduce the core-plus-PM losses. In addition, optimal location and orientation of the laminated PMs to the MFT core are explored to maximize their advantage in loss reduction. The following three factors are of great interest to the proposed method and their impact on the core-plus-PM losses of the S4T MFT can be figured out by comparing different configurations of the PMs depicted in Fig. 5:

1) use of laminated PMs compared to standard block PMs [cf., Fig. 5(d) and (f)];
2) locations of the PMs, either on the side or window plane of the core [cf., Fig. 5(b) and (d) for standard PMs while Fig. 5(c) and (e) for laminated PMs];
3) orientation of laminated PMs on the window plane, aligned with core lamination or not [cf., Fig. 5(e) and (f)].

All these factors are examined in 3-D-FEA simulation and experiments. Based on the observations, a generalized optimum design with laminated PMs will be concluded in the end. It should be pointed out that there is negligible variation in the

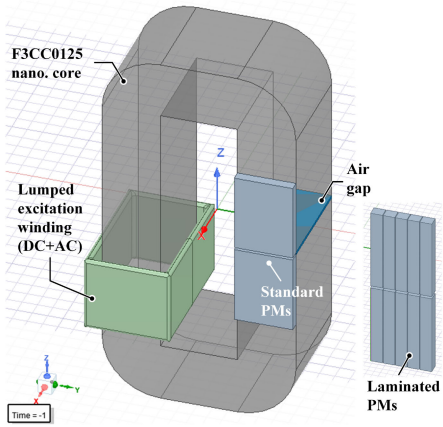

Fig. 6. Three-dimensional-FEA model in ANSYS Maxwell, including one pair of F3CC0125 nanocrystalline cores, a lumped winding for both dc and ac excitation, standard/laminated PMs with the same dimension on the core window plane (yz plane), and an air gap of 10 mils on one leg.

TABLE II
SPECIFICATIONS OF 3-D-FEA MODEL

Parameters	Values	Parameters	Values
Nanocrystalline core	F3CC0125	Air gap	10 mils
$B_{\mathrm{core,max}}$	1.23 T	$B_{\mathrm{pm,bias}}$	0.15 T/each
DC excitation	252 A	AC excitation	224 A @ 20 kHz
B_{dc}	0.59 T	B_{pp}	0.43 T @ 20 kHz

magnetic reluctance of all cases in Fig. 5 since the relative permeability of the sintered NdFeB PMs lies in the range 1.01–1.05, very close to the vacuum/air gap [26], [37], [38]. The resistivity of the PMs in use stays around 130–150 $\mu\Omega \cdot$ cm [39], [40].

V. THREE-DIMENSIONAL-FEA SIMULATION RESULTS

In this section, a 3-D-FEA model of the nanocrystalline core with standard and laminated PMs was implemented in ANSYS Maxwell to validate the proposed approaches. Next, the impact of standard and laminated PMs on core-plus-PM losses was compared at different operating points. Lastly, the effect of the number of lamination layers on the core-plus-PM losses was studied in FEA simulation. Please note that the laminated structure of the nanocrystalline core is not allowed to be modeled by Maxwell. Moreover, the loss breakdown in PMs is hardly attained limited by the built-in PM model in Maxwell.

A. Three-Dimensional-FEA Model

Fig. 6 depicts the 3-D-FEA model. The specifications of the model are summarized in Table II. The Nanocrystalline core F3CC0125 from Hitachi with standard and laminated PMs was modeled [39], [41]. An air gap of 10 mils on one leg was used. The same dimension of $1''\,\mathrm{L} \times 3/4''\,\mathrm{W} \times 1/8''\,\mathrm{H}$ was defined for both standard block PMs and laminated PMs. Five laminations with a lamination factor of 0.95 were defined for the laminated PMs. To save computation effort, a lumped excitation winding including both DC and AC excitation was modeled, where dc and 20 kHz triangular-shape ac excitation currents were superimposed. The flux density in the core was measured across the core area in the same core leg with the air gap.

TABLE III
LOSSES WITH STANDARD AND LAMINATED PMS IN FEA SIMULATION

PM configuration and $B_{\mathrm{PM,bias}}$		Core losses (W)	PMs losses (W)	Core-plus-PM losses (W)
No PMs	0	6.50	0	6.50
Standard	0.34 T	4.29	2.94	7.23
	0.52 T	4.42	3.22	7.64
	0.64 T	4.38	3.39	7.77
Laminated	0.30 T	4.73	0.57	5.30
	0.49 T	4.37	0.86	5.23
	0.61 T	4.44	1.03	5.47

By running the FEA simulation, the core-plus-PM losses with standard and laminated PMs were extracted and compared to validate the advantages of using laminated PMs in reducing core-plus-PM losses. The relationship between the core-plus-PM losses and different flux biases provided by the PMs $B_{\mathrm{PM,bias}}$ was investigated to draw a convincing conclusion, which will be presented in the next section.

In FEA simulation and subsequent hardware experiments, multiple PMs were stacked to provide enough $B_{\mathrm{PM,bias}}$ within the core area. Please note that a saturation effect of multiple stacked PMs on the total $B_{\mathrm{PM,bias}}$ they provide is expected for different configurations in Fig. 5, which can be extracted by FEA simulation to help quantity the experimental results.

B. Core-Plus-PM Losses With Standard and Laminated PMs

1) Core Loss Reduction With Added PMs: In the hybrid MFT of S4T converters, the PMs should be mounted in such a way that $B_{\mathrm{PM,bias}}$ counters the dc flux generated by windings, as explained in Section II. As a result, the net dc flux density in the core can be reduced, leading to an enhanced power transfer capability without increasing the core size.

Table III summarizes the core losses, PM losses, and total losses with/without standard and laminated PMs in FEA simulation at different operating points. The excitation currents and generated flux were kept the same under all cases for a meaningful comparison. Up to three pairs of standard and laminated PMs were stacked on the core window plane (yz plane in the 3-D-FEA model, the same definition for subsequent hardware experiments) to provide different $B_{\mathrm{PM,bias}}$.

For the base case without any PMs, an averaged 6.5 W of core losses were generated at $B_{\mathrm{PM,bias}} = 0\,\mathrm{T}$, including 4.7 W of hysteresis losses and 1.8 W of eddy-current losses. Compared with the base case, adding standard PMs decreases the core losses by 33% to around 4.36 W on average while adding laminated PMs reduces them by 30% to an average of 4.51 W. The 3% difference matches (3) considering the slight mismatch in $B_{\mathrm{PM,bias}}$ between these two types of PMs. In both cases, the reduction in the core losses results from the decreased net dc flux density in the core with added PMs. As shown in Fig. 7, compared with the core without any PMs, three laminated PMs in stack add a $B_{\mathrm{PM,bias}} = 0.61\,T$, and thus, decrease net flux density in the core overall despite a few high-density spots at the interface between core and PMs. In addition, the reduction

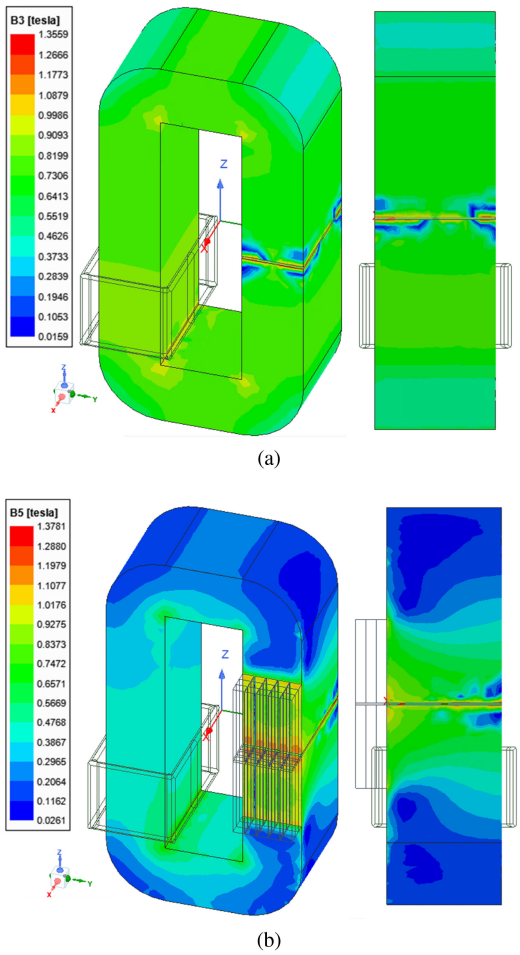

Fig. 7. Reduced flux density in the core with mounted PMs at peak excitation current. (a) Flux density in the core without any PMs. (b) Flux density in the core with three laminated PMs in stack. The net flux density decreased by 0.61 T with added PMs, leading to 30 % reduction in core losses.

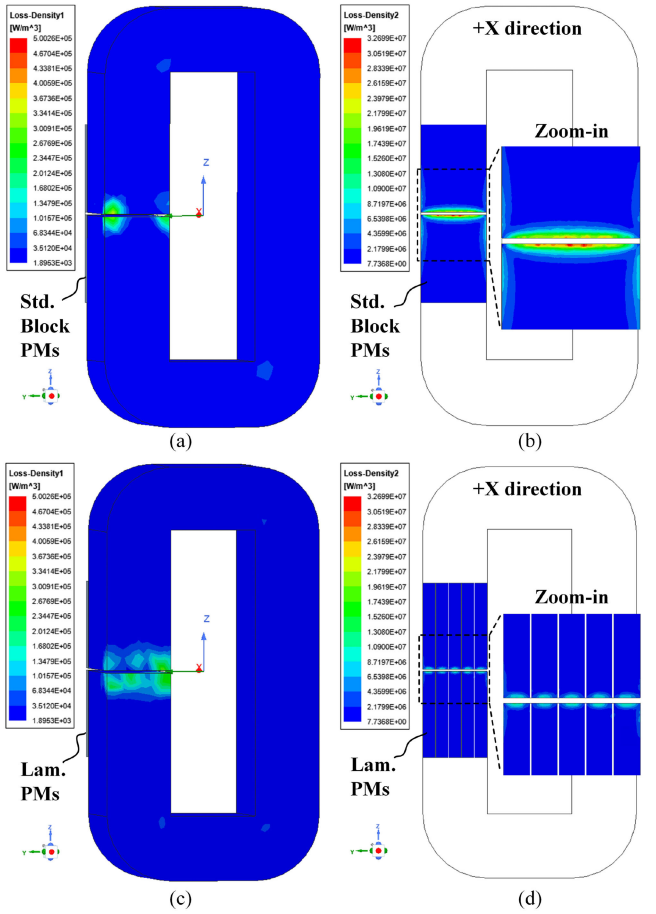

Fig. 8. Loss density of the core with one pair of standard and laminated PMs on the window plane in FEA simulation. (a) and (b) Loss density of the core and standard PMs. (c) and (d) Loss density of the core and laminated PMs (five lamination at a lamination factor of 0.95). Compared with the core with standard PMs, using laminated PMs reduces PM losses by 81% and core-plus-PM losses by 264%.

in core losses remains nearly constant with increased $B_{\mathrm{PM,bias}}$, indicating a saturation effect.

2) Core-Plus-PM Losses With Standard and Laminated PMs: Although both standard and laminated PMs can reduce the core losses in a similar extent, the impact of these two types of PMs on core-plus-PM losses is divergent.

In Table III, around 3.18 W of eddy-current losses on average are induced in standard PMs in total owing to the fringing effect, resulting in 7.54 W core-plus-PM losses with standard PMs. Thus, compared to the base case without any PMs, adding standard PMs increases the core-plus-PM losses by 16%. The significant eddy-current losses in the standard PMs would cause hot spots and eventually thermal runaway in the worst case, consistent with the thermal characterization results shown in Fig. 4.

In comparison, an averaged 0.82 W loss is induced in the selected laminated PMs, a reduction of 74% in eddy-current losses. As a result, adding laminated PMs generates 5.33 W core-plus-PM losses, a reduction of 18% than the base case. Compared to standard PMs, using laminated PMs lowers the core-plus-PM losses by 213% with

$$\Delta P_{\mathrm{loss}} = \frac{P_{\mathrm{loss,lamPM}} - P_{\mathrm{loss,stdPM}}}{P_{\mathrm{loss,stdPM}} - P_{\mathrm{loss,base}}} \tag{7}$$

which accounts for the impact of added PMs on core losses. This significant savings in the losses can mitigate the thermal stress of inductors/transformers in CSCs effectively and consequently relax their thermal design.

Fig. 8 shows the loss density of cores with one pair of standard and laminated PMs at the same excitation condition, where the PMs were mounted on the core window plane [cf., Fig. 5(d) and (f)]. Fig. 8(a) and (b) presents the loss density of the core with standard PMs while Fig. 8(c) and (d) presents the loss density of the core with laminated PMs. Laminated PMs exhibit 81% lower eddy-current losses in PMs and have an approximately 2.5 times lower loss density than standard PMs. As a result, laminated PMs decrease the core-plus-PM losses by 264% with (7). Theoretically, the benefits will continue to grow with the increased number of lamination layers and reduced thickness in each lamination, which will be validated in the next subsection.

TABLE IV
IMPACT OF THE NUMBER OF LAMINATION LAYERS ON PM LOSSES

Layers k	PM Losses (W)
3	1.23
5	0.54
10	0.20

C. Impact of the Number of Lamination Layers on PM Losses

In principle, laminated PMs can reduce the eddy-current losses by $1/k^2$, where k is the number of lamination layers. In this subsection, laminated PM losses with $k = 3/5/10$ were simulated and compared. The same lamination factor of 0.95 was applied to guarantee the same amount of magnetic materials for a meaningful comparison [36].

The results are summarized in Table IV. An exponential coefficient of 1.65 was extracted, around 20% lower than the theoretical value 2. The mismatch is attributed to the reduced volume of magnetic materials by the lamination factor of 0.95 and affected flux distribution by boundary conditions between lamination layers. In addition, the marginal reduction in eddy-current losses of laminated PMs decreases with the increased number of lamination layers in FEA simulation. Similarly, the benefits will saturate after a certain point in practice owing to lost magnetic materials and structural change during the laminating process as reported in [17] and [26].

VI. EXPERIMENTAL VALIDATION AND DISCUSSIONS

In addition to FEA simulations, experiments were also conducted to validate the proposed approach of using laminated PMs and their optimal location and orientation to reduce core-plus-PM losses. First, $B_{\mathrm{PM,bias}}$ of two types of PMs used in experiment were characterized by douple-pulse testing (DPT). Next, a three-winding method is introduced to measure the core-plus-PM losses. Lastly, the relationships of the core-plus-PM losses to various $B_{\mathrm{PM,bias}}$ for all configurations of interest are plotted and key observations were discussed.

A. $B_{\mathrm{PM,bias}}$ Characterization of Used Standard and Laminated PMs

1) Normalized $B_{\mathrm{PM,bias}}$ in the Core With Standard and Laminated PMs: Table V lists the BOM of key components in experiments.

A pair of Nanocrystalline core F3CC0125 from Hitachi Metals was selected [41]. The N42 standard PMs manufactured by K&J Magnetics feature a dimension of $1''\,\mathrm{L} \times 3/4''\,\mathrm{W} \times 1/8''\,\mathrm{H}$ [39]. The N50H laminated PMs with 30 lamination layers of 1 mm thickness were custom designed by Arnold Magnetic Technologies, presenting a dimension of $1.25'' \times 3/4''\,\mathrm{W} \times 1/16''\,\mathrm{H}$ [40]. Their pictures are shown in Fig. 10(a).

With an air gap of 10 mils, the saturation current of the F3CC0125 core was characterized to be 40 A by DPT [42]. Due to their different dimensions, the $B_{\mathrm{PM,bias}}$ provided by each PM was also characterized by DPT to guarantee a meaningful comparison in their impact on core-plus-PM losses. By sweeping the excitation current, a knee point in the $I-t$ curve can be captured, which was selected as the saturation current of the core under test I_{sat}. By adding one pair of standard or laminated PMs, I_{sat} will increase. As a result, the $B_{\mathrm{PM,bias}}$ provided by standard or laminated PMs can be calculated by scaling the change in saturation current ΔI_{sat} to I_{sat} with

$$\frac{B_{\mathrm{PM,bias}}}{B_{\mathrm{max,core}}} = \frac{\Delta I_{\mathrm{sat}}}{I_{\mathrm{sat}}}. \tag{8}$$

A $B_{\mathrm{PM,bias}} = 0.15\,\mathrm{T}$ was obtained for each pair of the standard PMs while 0.10 and $0.06\,\mathrm{T}$ for the custom laminated PMs in two different dimensions in Fig. 10(a).

2) Saturation Effect of Normalized $B_{\mathrm{PM,bias}}$ in the Core to Multiple Stacked PMs: To provide various values of $B_{\mathrm{PM,bias}}$ in each configuration, multiple PMs need to be stacked. The standard and laminated PMs used in experiment were modeled in ANSYS Maxwell and the effect of $B_{\mathrm{PM,bias}}$ on different number of PMs in stack under different configurations in Fig. 5 were simulated.

Fig. 9 plots the results, where the number of stacked PMs was selected up to twelve. The normalized $B_{\mathrm{PM,bias}}$ in the core was measured by the flux density changes across the core area, i.e., $B_{\mathrm{PM,bias}} = \Delta B_{\mathrm{Ac}}$. These saturation effects were used to quantify the impact of $B_{\mathrm{PM,bias}}$ on core-plus-PM losses at different operating points and validate the proposed idea of using laminated PMs to reduce core-plus-PM losses.

It can be observed that the standard PMs, no matter being placed on the side or core window plane, present an increased saturation effect than laminated PMs, featuring approximately

TABLE V
BOM OF KEY COMPONENTS IN EXPERIMENTS

Component	Manufacturer	Part Number
Nanocrystalline core	Hitachi	F3CC0125
Standard PMs	K&J Magnetics	BX0C2, Grade N42
Laminated PMs	Arnold Magnetic Technologies	Custom, Grade N50H

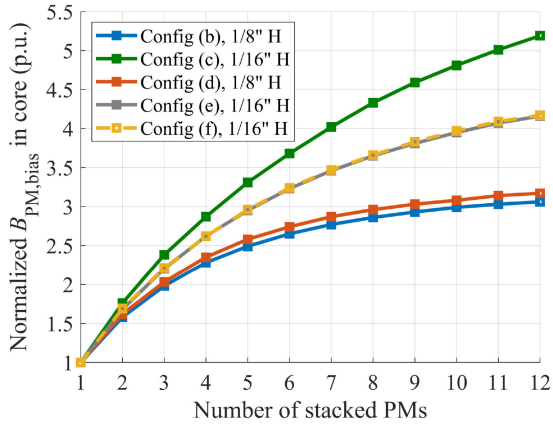

Fig. 9. Saturation effect of $B_{\mathrm{PM,bias}}$ to multiple PMs in stack under different configurations, given by 3-D-FEA simulation. Standard PMs suffer an increased saturation effect than laminated PMs, no matter on the side or window plane. For laminated PMs, their locations have an impact on the saturation effect while their orientations on the window side has little effect.

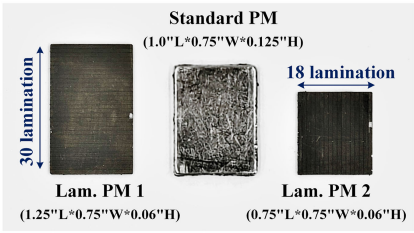

(a)

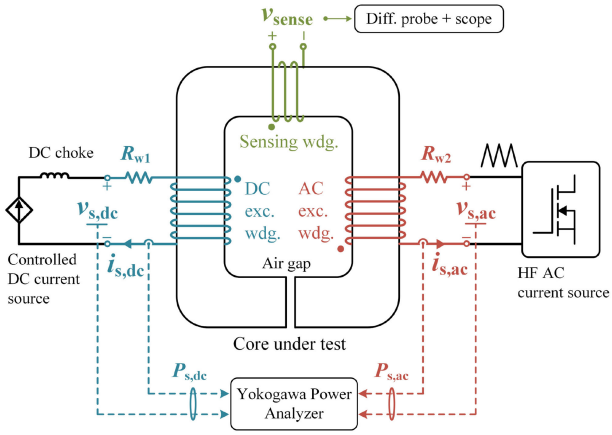

(b)

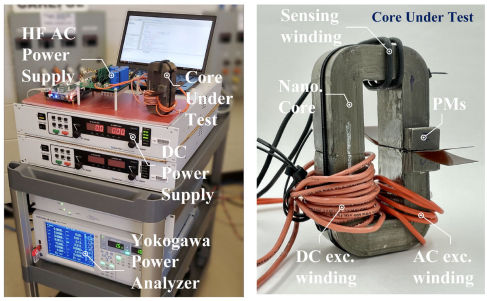

(c)

Fig. 10. (a) Pictures of standard and laminated PMs used in experiment. (b) and (c) Schematic and pictures of the test setup for core-plus-PM loss measurement.

$B_{\mathrm{PM,bias}} = 3\,\mathrm{p.u.}$ with twelve PMs in stack. The location of standard PMs has little impact on the normalized $B_{\mathrm{PM,bias}}$ in the core when comparing configuration (b) and (d).

In comparison, the laminated PMs feature a $B_{\mathrm{PM,bias}} > 5\,\mathrm{p.u.}$ when mounted on the side and $B_{\mathrm{PM,bias}} > 4\,\mathrm{p.u.}$ on the window plane. Different from standard PMs, the location of the laminated PMs affects its normalized $B_{\mathrm{PM,bias}}$ in the core, i.e., $\sim 20\%$ difference between configuration (c) and (e). Furthermore, the orientation of the laminated PMs on the window plane, aligning their lamination with core lamination or not, has a negligible effect on the normalized $B_{\mathrm{PM,bias}}$ in the core by looking at configuration (e) and (f).

The difference in the saturation effect of standard and laminated PMs should trace back to different geometries of these two PMs, leading to different magnetic reluctance of themselves. Thus, the ratios of magnetic reluctance between PMs and air gap are affected. This is another research topic and will not be discussed in this article.

TABLE VI
SPECIFICATIONS OF THE CORE AND PMS UNDER TEST

Parameters	Values
Saturation flux density B_{sat}	1.23 T
Air gap	10 mils
Saturation current	40 A
DC windings	AWG #12 * 12 turns
DC resistance of DC windings $R_{\mathrm{w1,dc}}$	28 mΩ
AC resistance of DC windings $R_{\mathrm{w1,ac}}$	407 mΩ @ f_{sw}
AC windings	AWG #12* 4 turns
DC resistance of AC windings $R_{\mathrm{w2,dc}}$	8 mΩ
AC resistance of AC windings $R_{\mathrm{w2,ac}}$	59 mΩ @ f_{sw}
Sensing coils/windings	AWG #12 * 2 turns
$B_{\mathrm{PM,bias}}$ of standard PM	0.15 T
$B_{\mathrm{PM,bias}}$ of laminated PM 1	0.10 T
$B_{\mathrm{PM,bias}}$ of laminated PM 2	0.06 T
DC flux bias B_{dc}	0.6 T
AC flux ripple ΔB_{pp}	0.43 T
Switching frequency f_{sw}	18 kHz

B. Methodology of Core-Plus-PMs Loss Measurement

Since the losses in the core and PMs are hard to decouple in experiment, a three-winding method was selected to measure the core-plus-PM losses as a whole [20]. Fig. 10(b) and Fig. 10(c) shows the schematic and test setup of loss characterization, respectively. The specifications of the core and PMs under test are summarized in Table VI.

Two excitation current sources are used to provide dc bias and a triangular-shape ac current ripple at 18 kHz, respectively. The dc and ac source power $P_{\mathrm{s,dc}}$ and $P_{\mathrm{s,ac}}$ were measured by power analyzer Yokogawa W1806 T. Hence, the core-plus-PM losses can be calculated by subtracting winding losses, P_{w1} and P_{w2} from the source power with

$$P_{\mathrm{loss,core}} = P_{\mathrm{s,dc}} + P_{\mathrm{s,ac}} - P_{\mathrm{w1}} - P_{\mathrm{w2}}. \tag{9}$$

The dc and ac winding losses can be calculated by

$$P_{\mathrm{w1}} = i^2_{\mathrm{s,dc(RMS)}} \cdot R_{\mathrm{w1,ac}} + \bar{i}^2_{\mathrm{s,dc}} \cdot R_{\mathrm{w1,dc}} \tag{10}$$

$$P_{\mathrm{w2}} = i^2_{\mathrm{s,ac(RMS)}} \cdot R_{\mathrm{w2,ac}}, \tag{11}$$

where the dc and ac resistance of two windings were measured by impedance analyzer and are listed in Table VI.

The peak-to-peak triangular-shape flux density ΔB_{pp} is measured and estimated by a sensing coil in experiments by

$$\Delta B_{\mathrm{pp}} = \frac{\hat{v}_{\mathrm{sense}}}{N_{\mathrm{sense}} \cdot A_{\mathrm{c}} \cdot 2 \cdot f_{\mathrm{sw}}} \tag{12}$$

where $\hat{v}_{\mathrm{sense}}$ is the peak magnitude of sensing voltage, $N_{\mathrm{sense}} = 2$ is the turns of sensing coil, and A_{c} is the core area. In experiments, $\Delta B_{\mathrm{pp}} = 0.43\,\mathrm{T}$ was maintained for all cases shown in Fig. 5.

C. Experimental Results

With the method discussed previously, the core-plus-PM losses with standard and laminated PMs under various configurations shown in Fig. 5 were measured to validate the effectiveness of the proposed approach. Multiple PMs were stacked to provide different $B_{\mathrm{PM,bias}}$ in each configuration, whose effective $B_{\mathrm{PM,bias}}$ can be obtained by mapping the

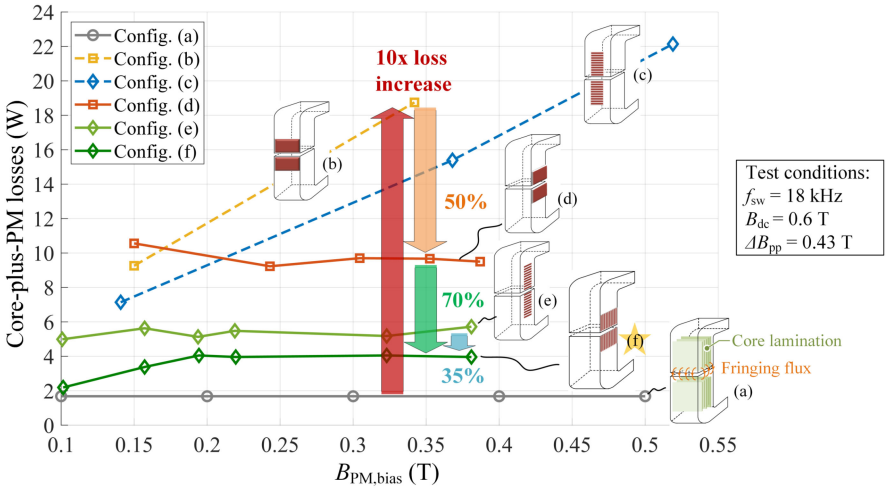

Fig. 11. Experimental results of core-plus-PM losses to different $B_{\mathrm{PM,bias}}$ under different configurations. Compared to the base case without any PMs, the initial MFT design with standard PMs on the side increases the core-plus-PM losses by more than ten times. In contrast, the proposed approach of using laminated PMs mounted on the window plane with aligned lamination with core reduces the core-plus-PM losses by 85%.

corresponding nonlinear curves that were simulated in Fig. 9. All other parameters can be found in Table VI.

Fig. 11 illustrates the core-plus-PM losses under different $B_{\mathrm{PM,bias}}$ for all configurations of interest, where the proposed approach of using laminated PMs is validated. The operating point at $B_{\mathrm{PM,bias}} = 0.35\,\mathrm{T}$ was selected as an example here to conduct a quantitative comparison to highlight the improvements by the proposed approach. In short words, the optimized design with the proposed approach in this article, as shown in configuration (f), reduced the core-plus-PM losses by 85% when compared to the initial design with standard PMs depicted in configuration (b).

At $B_{\mathrm{PM,bias}} = 0.35\,\mathrm{T}$, configuration (b) with standard PMs mounted on the side, which replicated the initial MFT design, increased the core-plus-PM losses by more than ten times than the base case without any PMs, resulting in tremendous thermal stress in magnetics.

To reduce the losses, the use of laminated PMs was proposed in this article. By comparing configuration (d) and (f), using laminated PMs lowered the core-plus-PM losses by 70% with (7) or its more general expression (13), validating the efficacy of the proposed approach

$$\Delta P_{\mathrm{loss}} = \frac{P_{\mathrm{loss,config2}} - P_{\mathrm{loss,config1}}}{P_{\mathrm{loss,config1}} - P_{\mathrm{loss,base}}}. \tag{13}$$

In addition, the impact of PMs' location on core-plus-PM losses is also of great interest. In Fig. 11, configuration (d) with standard PMs on the core window plane decreased the losses by 50% compared to configuration (b) with those on the side. Similar advantages were observed in laminated PMs when looking at configurations (c) and (e).

Lastly, an appropriate orientation of laminated PMs on the window plane is also shown to further reduce the losses. As presented in configuration (f), aligning the lamination of laminated PMs with the core lamination decreased the core-plus-PM losses by additional 35% in contrast to the case that they are not aligned shown in configuration (e) with (13).

D. Discussions and Practical Design Considerations

Based on 3-D-FEA simulation and experimental results, it is recommended to use laminated PMs, place them next to the air gap on the window plane, and orient their lamination aligned with core lamination. This configuration reduces the core-plus-PM losses to the most extent while increasing the saturation current significantly, featuring a general rule toward an optimum design.

Theoretically, placing bonded or sintered PMs right in the air gap can provide the maximum $B_{\mathrm{PM,bias}}$ in the core and increase the saturation current of the MFT. However, two concerns are preventing us from this implementation in practice. The first issue is the potential demagnetization of the PMs during fault conditions. A large opposing magnetic field would occur to the PMs and can exceed their intrinsic coercivity, leaving the converter operation in great uncertainty [31]. The other concern is the significant PM losses since they sit in the primary flux path instead of fringing flux, resulting in tremendous heat and a massive temperature rise. The high temperature will probably cause thermal demagnetization of the PMs and even a thermal runaway in the worst case. On the other hand, placing the PMs next to the air gap can significantly mitigate these two issues, escaping from the large fault current and primary flux in the core area.

Furthermore, in principle, the lamination thickness can be further reduced to tens of micrometers to decrease the eddy-current losses, especially for high-frequency applications. However, for the same volume of the PMs, an increased number of thinner lamination requires more electrically insulating film in between, leading to a reduced amount of effective magnetic materials. Moreover, the lamination manufacturing process aggravates the magnetic material loss and also generates numerous small grains

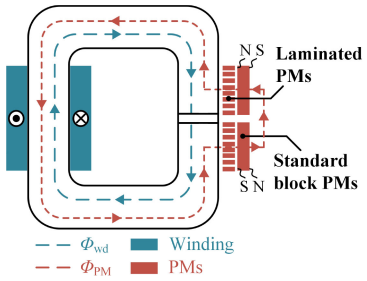

Fig. 12. Hybrid approach with laminated and standard PMs to balance the cost and performance.

around the PM surfaces, which might increase the hysteresis losses in return [17], [26].

Lastly, when looking closely at the FEA and experimental results, the core-plus-PM losses seem to increase and then saturate with increased $B_{\mathrm{PM,bias}}$ in the case of stacked magnets on the window plane, indicating a saturation effect of adding stacked PMs on the core-plus-PM losses. This observation allows a hybrid approach of applying laminated PMs next to the core and standard PMs on top of them, as illustrated in Fig. 12. This implementation is expected to reduce costs while maintaining the savings in losses, which can be validated in future work.

The difference in extents of improvement when using laminated PMs between 3-D-FEA simulation and experiments is probably caused by several factors. 1) The laminated structure of Nanocrystalline core was not able to modeled in the 3-D-FEA model but existing in the prototype, which affects the fringing flux distribution and induced losses. 2) Different dimensions and lamination factors of laminated PMs were used in FEA simulation and experiments. 3) The rigidity of selected wires fueled a loose coupling between the windings and the core in practice, resulting in an increased leakage flux and consequently a reduced flux density in the core at the same excitation currents. 4) Measurement error in power analyzer, especially under low power.

VII. Impact of Laminated PMs on 40 kVA S4T MFT

In the previous section, the proposed use of laminated PMs has been validated to reduce the losses significantly compared to standard PMs. In addition, adding laminated PMs can also offset the dc bias in the core, leading to reduced core size and cost for the same power transfer capability. In this section, the proposed use of laminated PMs is applied to a 40 kVA S4T MFT design to fully evaluate its advantages in saving the MFT cost and size.

Design specifications of the 40 kVA S4T MFT with/without laminated PMs are listed in Table VII. A picture of the 40 kVA S4T MFT prototype is shown in Fig. 13(a). The magnetizing inductance was designed to be 445 μH at 18 kHz. with the desired saturation current of 200 A, two sets of AMCC-630 equivalent nanocrystalline cores were selected, along with an air gap of 6 mm and 17 turns of copper foil windings.

A comparative evaluation of the saturation current and power losses was conducted for the 40 kVA S4T MFT with/without

TABLE VII
Design Specifications of the 40 kVA S4T MFT With/Without Laminated PMs

Parameters	w/o PMs	With PMs #1	With PMs #2
Power rating P_{n}		40 kVA	
Mag. inductance L_{m}		445 μH	
f_{sw}		18 kHz	
Nanocrystalline Core		AMCC-630	
Copper foil winding		17 turns	
Air gap		6 mm	
Laminated PMs	N/A	20	10 + 10
Saturation current	140 A	182 A	205 A
MFT losses	151 W	156 W	158 W

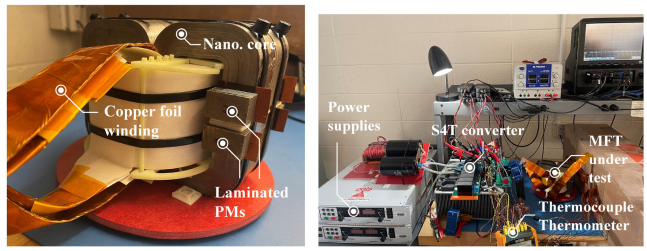

(a) (b)

Fig. 13. Picture of (a) 40 kVA S4T MFT prototype and (b) characterization test setup.

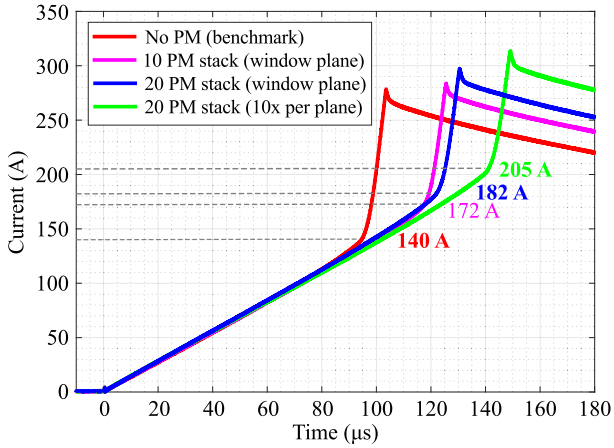

Fig. 14. Saturation current characterization of the 40 kVA S4T MFT with/without laminated PMs by DPT. Compared to the benchmark without PMs, a 46% increase in saturation current was achieved by placing 20 laminated PMs on two window planes. Furthermore, distributing 20 PMs on two window planes increases the saturation current by 23 A more than stacking 20 PMs on one window plane only, featuring another general rule of optimum design with laminated PMs.

laminated PMs. Fig. 13(b) exhibits the test setup and Fig. 14 presents the characterization results of the saturation current under difference cases. In traditional design without any PMs, the saturation current was characterized to be only 140 A, far less than the desired value. In comparison, the design with 20 custom laminated PMs on two window planes was measured to increase the saturation current by 46% to 205 A.

Furthermore, three more observations from Fig. 14 provide insight into the proposed approach and its optimal design. First, comparing three configurations with laminated PMs, namely 10/20 stacked PMs on a single window plane and 20 stacked

(a)

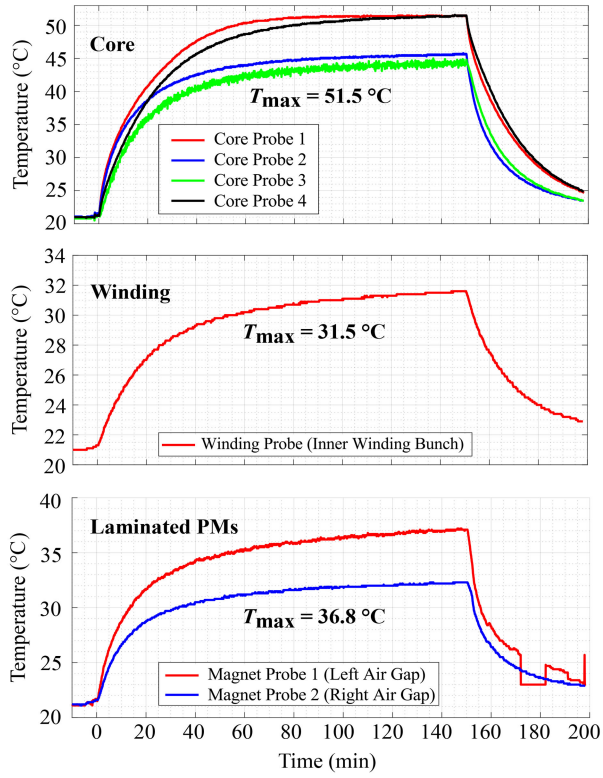

(b)

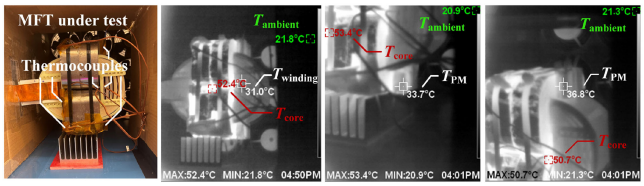

(c)

Fig. 15. (a) Power losses of the 40 kVA S4T MFT with laminated PMs at 30 kW measured by Yokogawa Power Analyzer W1806 T. (b) Thermal results of the S4T MFT core, windings, and laminated PMs after 2.5-hour continuous operation at 15 kW. (c) Thermal images of the S4T MFT core, windings, and laminated PMs after 2-hour continuous operation at 15 kW.

PMs evenly distributed on two window planes, the incremental changes in the saturation current validate the saturation effect of normalized $B_{\mathrm{PM,bias}}$ in the core to multiple stacked PMs presented in Fig. 9. Second, distributing 20 PMs on two window planes increases the saturation current by 23 A more than stacking 20 PMs on one window plane only, featuring another general rule of optimum design with laminated PMs. The difference is attributed to the saturation effect mentioned earlier. Lastly, the same slope before the core gets saturated suggests little change in magnetizing inductance and magnetic reluctance with $R_{\mathrm{m}} = N^2/L_{\mathrm{m}}$, where N is the number of turns of windings and is kept the same for all cases.

In addition to the saturation current, the power losses and thermal results of the MFT is another critical aspect to be inspected. Fig. 15(a) unveils the power loss measurement by Yokogawa Power Analyzer WT1806. Compared to 151 W losses in the traditional design without any PMs, the proposed design with 20 laminated PMs on two window planes increased the power losses by merely 5% to 158 W, adding negligible thermal stress to the cooling system while increasing the saturation current by 46%. Moreover, the small addition in MFT losses with 20 stacked laminated PMs than those with ten PMs suggests low losses induced in laminated PMs.

Fig. 15(b) plots temperature curves of the S4T MFT core, windings, and laminated PMs after 2.5-hour continuous operation at 15 kW and Fig. 15(c) shows thermal images after 2-hour running at 15 kW. Over the 2.5-hour continuous operation at 15 kW, the laminated PMs always present a lower temperature than the MFT core, suggesting a significant reduction in eddy-current losses compared to the standard PMs featuring a higher temperature than the core shown in Fig. 4.

VIII. Conclusion

In this article, the use of laminated PMs has been proposed to offset the dc flux while reducing eddy currents, leading to significant reductions in the size, cost, and losses of the flyback-type MFT in the S4T converters. Three-dimensional-FEA simulations and hardware experiments have been conducted to validate the effectiveness of the proposed approach. The impact of location, orientation, and distribution of the PMs on core-plus-PM losses is also explored, leading to a generalized minimum-loss design with laminated PMs. Finally, a comparative study of a 40 kVA S4T MFT has been conducted. Compared to the traditional design without any PMs, the proposed use of laminated PMs increased the saturation current by 46% with a merely 5% increase in MFT losses. Over the 2.5-hour continuous operation at 15 kW, laminated PMs always presented a lower temperature than the MFT core, suggesting a significant reduction in eddy-current losses compared to standard PMs.

To generalize the optimum design of the proposed approach, the laminated PMs are recommended to be placed on the window plane and be oriented in such a way that their laminations are aligned with the core laminations. Furthermore, instead of placing multiple laminated PMs stacked on one window plane only, distributing laminated PMs evenly on window planes provides extra benefits due to the mitigation in the saturation effect of $B_{\mathrm{PM,bias}}$ to multiple stacked PMs. Major observations in the 3-D-FEA simulations and experiments are presented as follows.

1) Compared to the core without any PMs, adding standard and laminated PMs of $B_{\mathrm{PM,bias}} = (0.5 \sim 1) \cdot B_{\mathrm{dc}}$ reduced core losses by 30% in the 3-D-FEA simulation.
2) Compared to standard block PMs, the use of laminated PMs (30 lamination $\times$ 1 mm thickness) reduced core-plus-PM losses by 85% in experiments, primarily benefiting from a significant reduction in eddy-current losses in the PMs.

3) It is beneficial to place PMs on the window plane of the core where the fringing flux around the air gap is expected to be relatively low. For both standard and laminated PMs, more than a 50% reduction in the core-plus-PM losses was measured in experiments when they were placed on the window plane rather than the side of the core, respectively.
4) Aligning the PM laminations (1 mm thickness) with the core laminations (0.012 mm thickness) led to an additional 35% reduction in core-plus-PM losses. Further improvement can be obtained with even thinner laminations or PMs based on powdered material.
5) The $B_{\mathrm{PM,bias}}$ suffers a saturation effect in the case of multiple stacked PMs, which has a negative impact on the core-plus-PM losses. Hence, distributing multiple PMs on different window planes was proven to mitigate this issue and provide enlarged benefits. This phenomenon also indicates that the first few magnets that are closest to the core dominate the eddy-current losses and core-plus-PM losses, providing an opportunity to use a hybrid approach of applying laminated PMs next to the core and standard PMs on top of them. This method can reduce cost while saving losses, which needs to be validated in future work.

ACKNOWLEDGMENT

This work was supported by the U.S. Department of Energy's Office of Energy Efficiency and Renewable Energy (EERE) under the Solar Energy Technologies Office Award Number DE-EE0008351. The views expressed herein do not necessarily represent the views of the U.S. Department of Energy or the United States Government.

The authors would like to thank the Center for Distributed Energy (CDE) at Georgia Tech for supporting this work.

REFERENCES

[1] R. A. Torres, H. Dai, W. Lee, B. Sarlioglu, and T. Jahns, "Current-source inverter integrated motor drives using dual-gate four-quadrant wide-bandgap power switches," *IEEE Trans. Ind. Appl.*, vol. 57, no. 5, pp. 5183–5198, Sep./Oct. 2021.

[2] M. Guacci *et al.*, "Three-phase two-third-PWM buck-boost current source inverter system employing dual-gate monolithic bidirectional GaN e-FETs," *CPSS Trans. Power Electron. Appl.*, vol. 4, no. 4, pp. 339–354, 2019.

[3] H. Dai, T. M. Jahns, R. A. Torres, D. Han, and B. Sarlioglu, "Comparative evaluation of conducted common-mode EMI in voltage-source and current-source inverters using wide-bandgap switches," in *Proc. IEEE Transp. Electrif. Conf. Expo.*, 2018, pp. 788–794.

[4] M. J. Mauger, P. Kandula, and D. Divan, "Soft-switching current source inverter for next-generation electric vehicle drivetrains," in *Proc. IEEE Transp. Electrif. Conf. Expo.*, 2020, pp. 651–658.

[5] Y. Xu, Z. Wang, P. Liu, Y. Chen, and J. He, "Soft-switching current-source rectifier based onboard charging system for electric vehicles," *IEEE Trans. Ind. Appl.*, vol. 57, no. 5, pp. 5086–5098, Sep./Oct. 2021.

[6] D. Zhang *et al.*, "Three-phase bidirectional buck-boost current DC-link EV battery charger featuring a wide output voltage range of 200 to 1000 V," in *Proc. IEEE Energy Convers. Congr. Expo.*, 2020, pp. 4555–4562.

[7] Y. Shi, R. Li, Y. Xue, and H. Li, "Optimized operation of current-fed dual active bridge DC-DC converter for PV applications," *IEEE Trans. Ind. Electron.*, vol. 62, no. 11, pp. 6986–6995, Nov. 2015.

[8] K. Mozaffari and M. Amirabadi, "A reduced-switch-count family of soft-switched high-frequency inductive AC-link converters," *IEEE Trans. Power Electron.*, vol. 35, no. 8, pp. 7972–7990, Aug. 2020.

[9] Z. An *et al.*, "Modular isolated soft-switching medium voltage string inverter for large-scale PV farm," in *Proc. IEEE Appl. Power Electron. Conf. Expo*., 2020, pp. 1067–1073.

[10] Z. An, R. P. Kandula, and D. Divan, "Feed-forward compensation for model predictive control in tri-port current-source medium-voltage string inverters for PV-plus-storage farms," in *Proc. IEEE Energy Convers. Congr. Expo.*, 2021, pp. 3430–3435.

[11] Y. Xu, Z. Wang, P. Liu, Q. Wei, F. Deng, and Z. Zou, "The modular current-fed high-frequency isolated matrix converters for wind energy conversion," *IEEE Trans. Power Electron.*, vol. 37, no. 4, pp. 4779–4791, Apr. 2022.

[12] H. Chen and D. Divan, "Soft-switching solid-state transformer (S4T)," *IEEE Trans. Power Electron.*, vol. 33, no. 4, pp. 2933–2947, Apr. 2018.

[13] L. Zheng *et al.*, "SiC-based 5-kV universal modular soft-switching solid-state transformer (M-S4T) for medium-voltage DC microgrids and distribution grids," *IEEE Trans. Power Electron.*, vol. 36, no. 10, pp. 11326–11343, Oct. 2021.

[14] D. Divan, Z. An, and P. Kandula, "Soft-switching-the key to high power WBG converters," in *Proc. Int. Power Electron. Conf.*, pp. 4001–4008, 2018.

[15] L. Zheng, R. P. Kandula, and D. Divan, "Soft-switching solid-state transformer with reduced conduction loss," *IEEE Trans. Power Electron.*, vol. 36, no. 5, pp. 5236–5249, May 2021.

[16] M. K. Kazimierczuk, *High-Frequency Magnetic Components*. Hoboken, NJ, USA: Wiley, 2009.

[17] W. Shen, F. Wang, D. Boroyevich, and C. W. Tipton, "Loss characterization and calculation of nanocrystalline cores for high-frequency magnetics applications," *IEEE Trans. Power Electron.*, vol. 23, no. 1, pp. 475–484, Jan. 2008.

[18] T. Guillod and J. W. Kolar, "Medium-frequency transformer scaling laws: Derivation, verification, and critical analysis," *CPSS Trans. Power Electron. Appl.*, vol. 5, no. 1, pp. 18–33, 2020.

[19] L. Zheng, R. P. Kandula, K. Kandasamy, and D. Divan, "New modulation and impact of transformer leakage inductance on current-source solid-state transformer," *IEEE Trans. Power Electron.*, vol. 37, no. 1, pp. 562–576, Jan. 2022.

[20] M. J. Mauger, X. Zheng, P. Kandula, and D. Divan, "Core losses of nanocrystalline materials under DC bias conditions," in *Proc. IEEE Appl. Power Electron. Conf. Expo.*, 2020, pp. 1–5.

[21] J. Muhlethaler, J. Biela, J. W. Kolar, and A. Ecklebe, "Core losses under the DC bias condition based on steinmetz parameters," *IEEE Trans. Power Electron.*, vol. 27, no. 2, pp. 953–963, Feb. 2012.

[22] H. Chen and D. Divan, "Design of a 10-kVA soft-switching solid-state transformer (S4T)," *IEEE Trans. Power Electron.*, vol. 33, no. 7, pp. 5724–5738, Jul. 2018.

[23] R. S. Yang, A. J. Hanson, B. A. Reese, C. R. Sullivan, and D. J. Perreault, "A low-loss inductor structure and design guidelines for high-frequency applications," *IEEE Trans. Power Electron.*, vol. 34, no. 10, pp. 9993–10005, Oct. 2019.

[24] P. Dowell, "Effects of eddy currents in transformer windings," in *Proc. Inst. Elect. Eng.*, vol. 113, no. 8, 1966, pp. 1387–1394.

[25] B. W. Carsten, "Inductor core shaping near an air gap," U.S. Patent 8 466 766, Jun. 18, 2013.

[26] D. Egorov *et al.*, "Hysteresis loss in NdFeB permanent magnets in a permanent-magnet-synchronous machine," *IEEE Trans. Ind. Electron.*, vol. 69, no. 1, pp. 121–129, Jan. 2022.

[27] A. Fukuma, S. Kanazawa, D. Miyagi, and N. Takahashi, "Investigation of AC loss of permanent magnet of SPM motor considering hysteresis and eddy-current losses," *IEEE Trans. Magn.*, vol. 41, no. 5, pp. 1964–1967, May 2005.

[28] J. Pyrhönen *et al.*, "Hysteresis losses in sintered NdFeB permanent magnets in rotating electrical machines," *IEEE Trans. Ind. Electron.*, vol. 62, no. 2, pp. 857–865, Feb. 2015.

[29] Y. Zhang, P. Pillay, M. Ibrahim, and M.-C. Cheng, "Magnetic characteristics and core losses in machine laminations: High-frequency loss prediction from low-frequency measurements," *IEEE Trans. Ind. Appl.*, vol. 48, no. 2, pp. 623–629, Mar./Apr. 2012.

[30] X. Han *et al.*, "Laminated permanent magnets enable compact magnetic components in current source converters," in *Proc. IEEE Energy Convers. Congr. Expo.*, 2021, pp. 5515–5522.

[31] H. Chen and D. Divan, "High-frequency transformer design for the soft-switching solid state transformer (S4T)," in *Proc. IEEE Appl. Power Electron. Conf. Expo*., 2017, pp. 2534–2541.

[32] MK Magnetics, "Tape wound core specialists," 2017, Accessed: Jan. 25, 2022. [Online]. Available: https://www.mkmagnetics.com/pdf/mk-brochure.pdf

[33] K&J Magnetics and A. Inc, "Block maganets BY0X02, NdFeB, grade N42," Accessed: Jan. 25, 2022. [Online]. Available: https://www.kjmagnetics.com/proddetail.asp?prod=BY0X02

[34] C. P. Steinmetz, "On the law of hysteresis," *Trans. Amer. Inst. Elect. Eng.*, vol. 9, no. 1, pp. 1–64, 1892.
[35] J. Reinert, A. Brockmeyer, and R. W. De Doncker, "Calculation of losses in ferro-and ferrimagnetic materials based on the modified Steinmetz equation," *IEEE Trans. Ind. Appl.*, vol. 37, no. 4, pp. 1055–1061, Jul.-Aug. 2001.
[36] N. Mohan, T. M. Undeland, and W. P. Robbins, *Power Electronics: Converters, Applications, and Design*. Hoboken, NJ, USA: Wiley, 2003.
[37] Advanced Magnets, "Sintered NdFeB magnets' specifications," Accessed: Apr. 18, 2022. [Online]. Available: https://www.advancedmagnets.com/wp-content/uploads/2020/07/Sintered-Neodymium-Iron-Boron-NdFeB-Magnets-Specifications.pdf
[38] S. Constantinides and D. Gulick, "NdFeB for high temperature motor applications," in *Proc. Motor Motion Assoc. Fall Tech. Conf.*, 2004, pp. 3–5.
[39] K&J Magnetics and A. Inc, "Block maganets BX0C2, NdFeB, grade N42," Accessed: Jan. 25, 2022. [Online]. Available: https://www.kjmagnetics.com/proddetail.asp?prod=BX0C2
[40] Arnold Magnetic Technologies, "N50H sintered neodymium-iron-boron (NdFeB) magnets," Accessed: Jan. 25, 2022. [Online]. Available: https://www.arnoldmagnetics.com/products/neodymium-iron-boron-magnets/, Rev. 210607
[41] H. Metals and A. Ltd, "FINEMET F3CC series cut core catalog," 2016, Accessed: Jan. 25, 2022. [Online]. Available: https://www.hitachi-metals.co.jp/products/elec/tel/pdf/hj-b11.pdf
[42] X. Han *et al.*, "Characterization of 3.3-kV reverse-blocking SiC modules for use in current-source zero-voltage-switching converters," *IEEE Trans. Power Electron.*, vol. 36, no. 1, pp. 876–887, Jan. 2021.

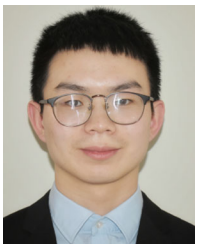

Zheng An (Student Member, IEEE) received the B.S. degree from Shanghai Jiao Tong University, Shanghai, China, in 2015, and the M.S. degree from RWTH Aachen University, Aachen, Germany, in 2017, both in electrical engineering. He is currently working toward the Ph.D. degree in electrical engineering with the Center for Distributed Energy, Georgia Institute of Technology, Atlanta, GA, USA.

From November 2016 to April 2017, he was an R&D Intern with Mercedes AG, Stuttgart, Germany, working on motor drives for Mercedes' premium EV. In the summer of 2021, he was a Power Electronics Intern with ABB U.S. Research Center, Raleigh, NC, USA, working on thermal characterization of SiC MOSFET. His research interests include grid integration of renewable energy, sustainable transportation, and application of wide-bandgap devices.

Mr. An was the recipient of the Outstanding Presentation Award at IEEE APEC 2022 in Houston, TX, USA. From July 2020 to July 2021, he served as the President of IEEE Power and Energy Society (PES) Student Chapter at Georgia Tech and led the chapter to be awarded as the Best Student Chapter across IEEE North America Region.

Xiangyu Han (Member, IEEE) received the B.Eng. degree in electrical engineering from Xi'an Jiao Tong University, Xi'an, China, in 2014 and the Ph.D. degree in the electrical and computer engineering from the Georgia Institute of Technology, Atlanta, GA, USA, in 2020.

From January to May 2020, he was an Intern with Tesla, Inc., CA, USA, where he is currently a Senior Electronic Design Engineer. His research interests include wide-bandgap power devices and applications of power electronics in power systems.

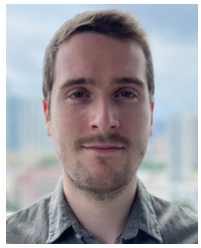

Mickael J. Mauger (Student Member, IEEE) received the M.S. degree (Diplôme d'Ingénieur) from ENSEEIHT, Toulouse, France, in 2015, and the M.S. degree in 2016 from the Georgia Institute of Technology, Atlanta, GA, USA, where he is currently working toward the Ph.D degree with the Center for Distributed Energy, all in electrical engineering.

In the summer of 2014, he was a Power Electronics Intern with the Electrical Power Converters (EPC) Group, CERN, Geneva, Switzerland, where he worked on high power converters for electromagnets of particle accelerators. In 2015, he was a Power Electronics Engineer with Thales Avionics, Valence, France, working on power converter designs for avionics equipment. He is currently the Director of Engineering with GridBlock, Atlanta, GA, USA, an Endeavour Energy company, where he is leading the development of a flexible, multiport energy router based on the S4T technology developed at the Center for Distributed Energy. His research interests include soft-switching converters, next-generation motor drives, multiport energy conversion, and grid-connected power electronics.

Brad Houska (Student Member, IEEE) received the B.S. degree in electrical engineering and the B.A. degree in physics from the University of Virginia, Charlottesville, VA, USA, in 2019, and the M.S. degree in electrical engineering in 2021 from the Georgia Institute of Technology, Atlanta, GA, USA, where he is currently working toward the Ph.D. degree with the Center for Distributed Energy.

His research interests include power electronics and magnetics.

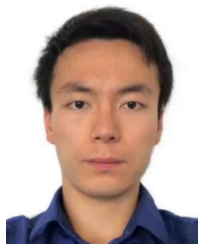

Decheng Yan (Student Member, IEEE) received the B.Sc. and M.Sc. degrees in electrical engineering from RWTH Aachen, Germany, in 2016 and 2019, respectively. He is currently working toward his Ph.D. degree in electrical engineering with the Center for Distributed Energy, Georgia Institute of Technology, Atlanta, GA, USA.

From November 2017 to April 2018, he was a Research Intern with Bosch GmbH, Renningen, Germany, where he worked on fault detection and classification of permanent-magnet synchronous machines (PMSM). His research interests include grid-interactive next-generation power converters, high-performance controllers for current-source inverters, and power system stability.

Mr. Yan was the recipient of the second prize paper award in 2021 from the IAS Annual Meeting (IACC-IAS).

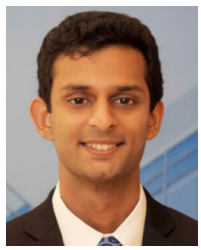

Aniruddh Marellapudi (Student Member, IEEE) received the B.S. degree in biomedical engineering from Duke University, Durham, NC, USA, in 2017, and the M.S. degree in electrical engineering in 2020 from the Georgia Institute of Technology, Atlanta, GA, USA, where he is currently working toward the Ph.D. degree in electrical engineering with the Center for Distributed Energy.

In the summer of 2019, he worked with the Duke Electric Vehicles team to set the Guinness World Record for "Most Efficient Prototype Electric Vehicle" with an efficiency of 797 mi/kWh (27 482 MPGe). Also in the summer of 2019, he was an Intern with Wolfspeed, Durham, NC, USA, where he studied the impacts of nano-henry inductances in SiC MOSFET switching characterization testbeds. He is currently a Power Electronics Engineer with Endeavour Inspired Infrastructure, Atlanta, GA, USA, where he is designing the GridBlock, a plug-and-play, 500 kW multiport energy router. His research interests include grid-connected power electronics, renewable energy integration, and understanding optimal pathways to achieving 100% energy sustainability.

Joseph Benzaquen (Member, IEEE) received the B.Sc. and M.Sc. degrees in electrical engineering from Universidad Simón Bolívar, Caracas, Venezuela, in 2011 and 2015, respectively, and the Ph.D. degree in electrical engineering from Smart Power Electronics & Control Systems (SPECS), Kansas State University, Manhattan, KS, USA, in 2020.

He is currently working as the Chief Research Engineer with the Center for Distributed Energy, Georgia Institute of Technology, Atlanta, GA, USA, where he initially joined in Fall 2020 as a Postdoctoral Fellow. His research interests include grid-interactive next-generation power converters and high-performance controllers for e-mobility power converters.

Rajendra Prasad Kandula (Member, IEEE) received the B.E. degree from the National Institute of Technology, Nagpur, India, in 2002, the M.E. degree from the Indian Institute of Science, Bangalore, India, in 2004, and the Ph.D. degree from the Georgia Institute of Technology, Atlanta, GA, USA, in 2014, all in electrical engineering.

He worked for three years with Bharat Heavy Electricals Limited (BHEL) R&D, Hyderabad, India, as a Design Engineer in the area of industrial drives and PV applications. He worked with Varentec, Santa Clara, CA, USA, as a Principal Engineer, mainly working in the area of development of power flow controllers and hybrid transformers for meshed transmission systems. He worked as a Chief Engineer with Center for Distributed Energy, Georgia Tech, Atlanta, GA, USA, from 2015 to 2021. He is currently working as an R&D Staff Scientist with Oak Ridge National Laboratory, Oak Ridge, TN, USA. His main research interests include applications of power electronics for utility applications such as hybrid transformers, solid state transformers, fast EV chargers, grid-forming converters, etc.

Deepak Divan (Life Fellow, IEEE) received the B.Tech. degree from the Indian Institute of Technology Kanpur, Kanpur, India, in 1975, and the M.Sc. and Ph.D. degrees from the University of Calgary, Calgary, AB, Canada, in 1979 and 1983, respectively, all in electrical engineering.

He is currently John E. Pippin Chair Professor, GRA Eminent Scholar, and the Director of the Center for Distributed Energy, Georgia Institute of Technology, Atlanta, GA, USA. He works closely with utilities, industry, and is actively involved in research, teaching, entrepreneurship, and starting new ventures. He has started several companies, including Varentec, Santa Clara, CA, USA, where he served as a Founder, the President, and the CTO from 2011 to 2014, and as a Chief Scientist for several years after. He led the company as it developed its suite of innovative distributed real-time grid control technologies. Varentec was funded by leading green-tech Venture Capital firm Khosla Ventures and renowned investor Bill Gates. He has founded or seeded several new ventures, including Soft-Switching Technologies, Innovolt, Varentec, and Smart Wires, which together have raised >$160 M in venture funding. He has 40 years of academic and industrial experience, 75 issued and pending patents, and over 400 reviewed publications. His research interests include power electronics, power systems, smart grids, and distributed control of power systems.

Dr. Divan is an Elected Member of the U.S. National Academy of Engineering, the National Academies Board on Energy and Environmental Systems, and the NASEM Committee on the Future Grid. He was a Past President of the IEEE Power Electronics Society. He was the recipient of the IEEE William E. Newell Power Electronics Award and International Steering Committee Chair of the IEEE Empower a Billion Lives global competition to crowdsource scalable energy access solutions.